Synthesis and Electrochemical Properties of Two-Dimensional Hafnium Carbide

Jie Zhou, Xianhu Zha, Xiaobing Zhou, Fanyan Chen, Guoliang Gao, Shuwei Wang, Cai Shen, Tao Chen, Chunyi Zhi, Per Eklund, Shiyu Du, Jianming Xue, Weiqun Shi, Zhifang Chai and Qing Huang

Zhou, J., Zha, X., Zhou, X., Chen, F., Gao, G., Wang, S., Shen, C., Chen, T., Zhi, C., Eklund, P., Du, S., Xue, J., Shi, W., Chai, Z., Huang, Q., (2017), Synthesis and Electrochemical Properties of Two-Dimensional Hafnium Carbide, *ACS Nano*, 11(4), 3841-3850.
https://dx.doi.org/10.1021/acsnano.7b00030

Synthesis and Electrochemical Properties of Two-Dimensional Hafnium Carbide

Jie Zhou,[§,⁄,†] Xian-Hu Zha,[§,†] Xiaobing Zhou,[§] Fanyan Chen,[§] Guoliang Gao,[η] Shuwei Wang,[η] Cai Shen,[η,] Tao Chen,[§] Chunyi Zhi,[‡] Per Eklund,[ξ] Shiyu Du,[§,*] Jianming Xue,[η] Weiqun Shi,[ζ] Zhifang Chai,[ζ] and Qing Huang,[§,*]*

[§] Engineering Laboratory of Specialty Fibers and Nuclear Energy Materials, Ningbo Institute of Materials Engineering and Technology, Chinese Academy of Sciences, Ningbo, Zhejiang 315201, China.

[⁄] University of Chinese Academy of Sciences, 19A Yuquan Road, Shijingshan District, Beijing 100049, China.

[η] Energy Storage Division, Ningbo Institute of Materials Engineering and Technology, Chinese Academy of Sciences, Ningbo, Zhejiang 315201, China.

[‡] Department of Physics and Material Science, City University of Hong Kong, Kowloon, Hong Kong SAR, China.

[ξ] Thin Film Physics Division, Linköping University, IFM, 581 83 Linköping, Sweden.

[η] State Key Laboratory of Nuclear Physics and Technology, CAPT and IFSA Collaborative Innovation Center of MoE, Peking University, Beijing 100871, China.

[ζ] Laboratory of Nuclear Energy Chemistry and Key Laboratory for Biomedical Effects of Nanomaterials and Nanosafety, Institute of High Energy Physics, Chinese Academy of Sciences, Beijing 100049, China.

[†] These authors contributed equally to this work.

Keywords: *MXenes, selective etching, 2D materials, DFT calculations, electrochemical properties*

Abstract: We demonstrate fabrication of a two-dimensional Hf-containing MXene, $Hf_3C_2T_z$, by selective etching of a layered parent $Hf_3[Al(Si)]_4C_6$ compound. A substitutional solution of Si on Al sites effectively weakened the interfacial adhesion between Hf-C and Al(Si)-C sub-layer within the unit cell of the parent compound, facilitating the subsequent selective etching. The underlying mechanism of the Si-alloying-facilitated etching process is thoroughly studied by first-principles density functional calculations. The result showed that more valance electrons of Si than Al weaken the adhesive energy of the etching interface. The MXenes were determined to be flexible and conductive. Moreover, this 2D Hf-containing MXene material showed reversible volumetric capacities of 1567 mAh cm^{-3} and 504 mAh cm^{-3} for lithium and sodium ions batteries, respectively, at a current density of 200 mAg^{-1} after 200 cycles. Thus, $Hf_3C_2T_z$ MXenes with 2D structure is a candidate anode material for metal-ion intercalation, especially for applications where size matters.

Graphene has many exciting properties but is restricted in some applications such as field-effect transistor by its relatively simple chemistry and intrinsic zero bandgap.[1, 2] Therefore, investigations on other 2D materials with abundant elemental composition, such as metal oxides,[3] layered metal chalcogenides (LMDCs),[4] hexagonal boron nitride (BN),[5] and hydroxides[3, 6] are of great interest. Since 2011, a new group of 2D transition metal carbides and nitrides labeled MXenes have been developed.[7-10] Generally, they are fabricated by selectively etching of the A-layers from their 3D layered parent $M_{n+1}AX_n$ phases, where M is an early transition metal, A is an A-group element, such as Al or Si, X is carbon and/or nitrogen, and n = 1, 2, or 3.[11] To date, synthesized MXenes include $Ti_3C_2T_z$, Ti_2CT_z, $Ta_4C_3T_z$, $TiNbCT_z$, $(V_{0.5},Cr_{0.5})_3C_2T_z$, Ti_3CNT_z, Nb_2CT_z, V_2CT_z, $Nb_4C_3T_z$, $Mo_2TiC_2T_z$, $Mo_2Ti_2C_3T_z$, $Cr_2TiC_2T_z$, Mo_2CT_z, $Ti_4N_3T_z$, $(Nb_{0.8}, Ti_{0.2})_4C_3T_z$, $(Nb_{0.8}, Zr_{0.2})_4C_3T_z$, $Mo_2ScC_2T_z$, and $Zr_3C_2T_z$[7, 8, 12-21] where T_z represents surface groups, generally O, OH, and F. MXenes generally have high specific surface areas, favorable conductivity and hydrophilic surfaces, high elastic moduli and carrier mobility,[22-26] and low metal diffusion barriers on their surfaces.[27] Thus, MXenes are predicted to have possible applications in electrochemical energy storage and functional polymer composites.[28-33] To further enrich the MXene family, more efforts should be made to synthesize potential MXenes in system where their parent Al-containing MAX phases are not easy to establish, such as Zr, Hf and Sc-containing MXenes. While there are a few very recent reports on MAX phases in the Zr-Al-C and Hf-Al-C systems,[34-36] it is noteworthy that the transition metals Zr and Hf are more inclined to form a new family of layered ternary and quaternary transition-metal carbides beyond the MAX phases, and hold a common formula of $(MC)_nAl_3C_2$ and $(MC)_n[Al(Si)]_4C_3$ (where M= Zr or Hf, n = 1-3).[37] The crystal structure can be viewed as alternating stacking of NaCl-type MC layers and Al_4C_3-like Al_3C_2/$[Al(Si)]_4C_3$ units, and an

atomic layer of carbon atoms are shared at their coupling boundary. Very recently, we have synthesized the Zr-containing MXene through selective etching of Al-C units from layered $Zr_3Al_3C_5$.[13] Of special interest to this work is the synthesis and characterization of the Hf-containing MXenes. In contrast to $Zr_3Al_3C_5$, the interfacial bonds between M-C and Al-C layers are relatively strong in the layered Hf-Al-C carbides.[37] Thus, it is difficult to directly exfoliate ternary Hf-Al-C carbides into MXenes simply by selective etching. Xie *et al.* [38] found that the solid solution of Si-Al in the A layer of Ti_3SiC_2 weakened the bonds and facilitated the exfoliation of $Ti_3(Si_{0.75}Al_{0.25})C_2$, but the underlying mechanism is not well understood. Since the selective etching process is based on the difference in reactivity and stability between the different fractions of the original material,[10] activating the Al-C sub-layer and effectively weakening the interfacial adhesion between Hf-C and Al-C sub-layers would be beneficial to realize the selective etching process. Here, we instead alloy the ternary Hf-Al-C carbide with Si on Al sites,[39] forming a $Hf_3[Al(Si)]_4C_6$ solid solution. Then, the exfoliation of Si-containing solid solution by selective etching of [Al(Si)]-C sub-layer in concentrated hydrofluoric acid (HF) is realized to form $Hf_3C_2T_z$ MXene. Combining with first-principles density functional calculations, the underlying mechanisms of the Si-alloying facilitated etching process, and the structural, mechanical and electronic properties of the as obtained 2D carbide are investigated. Furthermore, the application of $Hf_3C_2T_z$ MXene as anode materials for rechargeable batteries with long cycling performance is explored.

Results and Discussion

The $Hf_3[Al(Si)]_4C_6$ and Hf-Al-C composite powders were synthesized by an *in situ* reactive pulsed electric current sintering (PECS) process similar to our previous study.[40] Then the subsequent exfoliation process was carried out by using concentrated HF. The as-synthesized

powders are mainly composed of $Hf_3[Al(Si)]_4C_6$ besides a small amount of $Hf_2[Al(Si)]_4C_5$ and rock-salt-like cubic HfC secondary phase (Figure 1a, black). When the as-fabricated powders were added in a 35 wt % HF aqueous solution, bubbles were observed, possibly to be CH_4 or H_2, which had also been observed during the fabrication process of $Zr_3C_2T_z$ and $Ti_3C_2T_z$ MXenes from corresponding $Zr_3C_3C_5$ and Ti_3AlC_2 precursors reported previously.[7, 8] XRD pattern of the etched material, in its vacuum-dried state, show the intensity of diffraction peaks belonging to the parent $Hf_3[Al(Si)]_4C_6$ is weakened substantially after immersion in the concentrated HF solution (Figure 1e, red). The (0003) peak downshift to a lower angle of $2\theta = 5.4°$, attributing to an increased *c* lattice parameter of 32.70 Å, from the original 31.88Å ($2\theta = 5.54°$) of $Hf_3[Al(Si)]_4C_6$ crystal (see magnified view in Figure 1f). Concomitantly, another newly emerged two (000l) peaks located at lower angles of $2\theta = 16.25°$, and $2\theta = 27.32°$ can be detected, respectively, which also show a downshift of about 0.14° from original $Hf_3[Al(Si)]_4C_6$ crystal (Figure S9). The three newly formed lower angle (000l) peaks are similar to our previously reported work on $Zr_3C_2T_z$ MXene, and is also typical for most HF-etched MXenes from parent MAX phases. Moreover, some unreacted $Hf_3[Al(Si)]_4C_6$, together with a small amount of cubic HfC can also be detected. The significant decrease of the peaks belonging to parent $Hf_3[Al(Si)]_4C_6$ crystal and the three newly formed lower angle (000l) peaks implied that the sample was partially converted to MXene. Unlike the broad peaks typical of HF-etched MXene from MAX phases precursors,[8, 16, 22] all (000l) peaks observed in our present study exhibit sharper shape and increased intensity, similar to our previously work on the preparation of $Zr_3C_2T_z$ MXene, which is more typical of intercalated MXenes.[29, 41] The enlarged c lattice parameter might be associated with spontaneous intercalation of water and other etched-out product during the etching process. Meanwhile, the (0003) peak ($2\theta = 6.58°$) originating from the

$Hf_2[Al(Si)]_4C_5$ secondary phase broadens and downshifts to a lower angle of 2θ =6.37°(Figure 1a and 1b), which implies that $Hf_2[Al(Si)]_4C_5$ converted into MXenes after the HF treatment as well. Furthermore, in contrast with the peaks with large downshift in most HF-etched MXenes,[7, 16] a lower degree of downshift of (000l) peaks in our current study is likely because of the selective etching of [Al(Si)]C slabs, which are much thicker than the A-layers in MAX phases.

SEM images of $Hf_3[Al(Si)]_4C_6$ before and after the HF treatment are shown in Figure 1c and 1d, respectively. The as-synthesized $Hf_3[Al(Si)]_4C_6$ phase exhibits a typical lamellar morphology (Figure 1c). In contrast, delaminated few layered thin flakes with large lateral size (2-5μm) (Figure 1d) are observed in the HF etched material after mild sonication and centrifugation. The corresponding EDS analysis of the flakes show the presence of Hf, C, O, F, but disappearance of the Al, and Si signals (Figure S1c in supporting information, SI). Additionally, the obtained Hf:[Al(Si)] ratio was about 3.0:1.3 (Figure S1a-b) from an area of about 2000 μm^2 of the as-etched powders, implying that more than 65% of the $Hf_3[Al(Si)]_4C_6$ phase was converted into $Hf_3C_2T_z$.[16] Moreover, X-ray photoelectron spectroscopy (XPS, **Figure** S4-S5) results in the Al 2p region, Si 2p region, and C 1s region show significantly decrease in the content of Al(Si)-C bonding after HF treatment (Figure S4-S5), which suggests that the selective etching of Al(Si)-C layer from the primitive unit cell has occurred. Concomitantly, fitted XPS results in Hf 4f region and O1s region also show evidence of Hf–F and Hf–O bonding (Figure S2-S3), suggests the presence of $Hf_3C_2T_z$ layers with O- and F-containing surface terminations, as has been characterized for HF-produced MXenes previously.[42] It is interesting to note that the multilayered $Hf_3C_2T_z$ materials obtained in our current study are able to delaminate and form a stable colloidal solution in deionized water (insets in Figure S1c) without pre-treatment with an additional intercalate agent. However, in most previously reported HF-etched multilayer

MXenes,[8, 22] a preceding intercalation of species between the layers before sonication is need to obtain the corresponding colloidal suspension of single/few layered MXenes.[9, 41, 43] Thus it is reasonable to speculate that the residual force in HF etched multi-layered $Hf_3C_2T_z$ might be more weakly than those of previously reported MXenes. In our current study, the weakened interface binding between the Hf-C and Al(Si)C sub-layers induced by substitution might be beneficial to the delamination of as-synthesized multilayer $Hf_3C_2T_z$ MXenes in deionized water. Moreover, our calculated results (Figure S6) show that multilayer $Hf_3C_2F_2$ MXene has the relatively lower adhesive energy when compared with that of typical $Ti_3C_2F_2$ MXene. Thus, the as-synthesized Hf-containing MXene with multilayer configuration is readily to be delaminated in solution, and the detailed discussion is given in the SI. TEM micrographs and EDS analysis of the HF-treated $Hf_3[Al(Si)]_4C_6$ powders after sonication and centrifugation are shown in Figure 1e-g, thin flakes with scrolled behavior can be observed (Figure 1e), and corresponding EDS results confirm the presence of Hf, C, and O signals (Figure 1g). The selected area electron diffraction (SAED, inset in Figure 1e) patterns of the two overlapping flakes with a slight difference in orientation demonstrates the hexagonal symmetry.[37] Figure 1f shows stacked bilayer MXene sheets, and the thickness of a monolayer sheet is estimated to be about 1.2 nm, demonstrating that the obtained material is indeed two-dimensional.

On the contrary, bare ternary Hf-Al-C composite powders cannot be selectively etched into Hf-containing MXenes in HF solutions even with different concentrations (Table S3). According to the XRD results shown in Figure 2a, the as-fabricated Hf-Al-C powders are composed of $Hf_3Al_4C_6$, $Hf_2Al_4C_5$, and $Hf_3Al_3C_5$ phases, after HF treatment, the mainly etching product is cubic HfC phase (Figure 2a). Figure 2c and 2d show the SEM morphologies of the etched powders, where particles with an average size of about 200 nm can be observed. The

corresponding EDS analysis shown in Figure 2b indicates the presence of mainly Hf and C elements. The corresponding molar ratio of Hf:C approximate 1:1, which is consistent with the aformentioned XRD results.

Figure 3a shows an AFM topography image of delaminated $Hf_3C_2T_z$ sheets deposited on Highly Oriented Pyrolytic Graphite (HOPG) substrate. Interestingly, a neat surface of $Hf_3C_2T_z$ flakes can be easily formed on HOPG surface (Figure 3a). The flakes have a thickness similar to that of bilayer MXene (Figure 3b). In addition, the $Hf_3C_2T_z$ flakes can replicate the steps of the HOPG surface, which implies its mechanical flexibility and affinitive to graphite. It is thus reasonable to speculate that delaminated $Hf_3C_2T_z$ or hybrid structures there of combined with graphene or other 2D materials may be useful in flexible and stretchable electronics. [44, 45]

According to XPS results (Figure S2-S5) and our previous theoretical work on $Zr_3C_2T_z$ MXene,[13] we have determined that the shared carbon atomic plane between the Hf-C and Al-C sublayers in $Hf_3Al_4C_6$ [or $Hf_3[AlSi]_4C_6$] unit cell shown in Figure 4a is also etched away, which means the reaction products are $Hf_3C_2T_z$ MXenes. Thus, the etching interface exists between the Hf and C atomic planes as the red dashed line shown in Figure 4b, where the Hf-C bonds are broken during etching. Regarding to the etching process, an important issue that needs to be figure out is why the introduction of silicon can significantly accelerate the etching of the layered ternary carbide $Hf_3Al_4C_6$. In order to understand this behavior, the adhesive energy between two detached layers which directly implies the strength of the layer interaction is first investigated. Seen from the atomic configuration of $Hf_3Al_4C_6$ as shown in Figure 4a, the supercell is comprised by three monomers stacking along the c-axis. Therefore, to reduce the large computational cost of DFT calculations, a representative monomer (shown in Figure 4b) rather than the entire unit cell is adopted to investigate the adhesive energy. The Hf_3C_2 and Al_4C_4 can

be assumed as the two detached layers after the HF etching, and the adhesive energy between the two layers is defined as:

$$E_{adhesive} = \frac{1}{A}(E_{Hf_3C_2} + E_{Al_4C_4} - E_{Hf_3Al_4C_6}) \quad (1)$$

where $E_{adhesive}$ denotes the adhesive energy, and $E_{Hf_3C_2}$, $E_{Al_4C_4}$ and $E_{Hf_3Al_4C_6}$ are the total energies of the Hf_3C_2, Al_4C_4 layers and $Hf_3Al_4C_6$ monomer, respectively. A denotes the area of etching interface. In view of the substitution of silicon, a 2×1×1 supercell with an aluminum atom replaced by silicon is adopted. The substitution of silicon respectively in the top and second aluminum layers are studied considering the structural symmetry, as shown in Figure 4c and 4d. Similarly, the adhesive energies for the interfaces (denoted in red dashed lines) of these $Hf_3Al_{3.5}Si_{0.5}C_6$ are also studied. All the chemical equations for etching behaviors and corresponding adhesive energies are given in Table 1, where the subscripts "t" and "s" are adopted to distinguish the silicon position in the top and the second aluminum layers, respectively. Evidently, the adhesive energy is reduced drastically through silicon substitution, especially in the $Hf_3Al_{3.5}Si_{0.5t}C_6$ configuration with an aluminum atom in the top-layer replaced by silicon. For the pure $Hf_3Al_4C_6$ monomer, the adhesive energy between the two detached layers is 0.442 eV/Å^2, and which reduces to 0.211 eV/Å^2 in $Hf_3Al_{3.5}Si_{0.5t}C_6$. These data explain our experimental results, and imply that the accelerated etching behavior is mainly caused by the silicon substitution in the top aluminum layer. It is noteworthy that here the silicon alloying effect is elaborated based on the 2×1×1 supercell for simplicity. To be more convinced, more diluted silicon alloying ratios with an aluminum atom replaced by silicon based on those 3×1×1 ($Hf_3Al_{3.67}Si_{0.33t}C_6$) and 2×2×1 ($Hf_3Al_{3.75}Si_{0.25t}C_6$) supercells have also been investigated. The corresponding adhesive energies are giving in Table 1 as well. Evidently, silicon alloying can

effectively reduce the adhesive energy of the etching interface, and the reduced magnitude of adhesive is proportional to the alloying ratio.

Table 1. The chemical equations for etching behaviors and corresponding adhesive energies (in eV/Å^2).

Etching processes	Adhesive energies
$Hf_3Al_4C_6 \rightarrow Hf_3C_2 + Al_4C_4$	0.442
$Hf_3Al_{3.5}Si_{0.5t}C_6 \rightarrow Hf_3C_2 + Al_{3.5}Si_{0.5t}C_4$	0.211
$Hf_3Al_{3.5}Si_{0.5s}C_6 \rightarrow Hf_3C_2 + Al_{3.5}Si_{0.5s}C_4$	0.283
$Hf_3Al_{3.67}Si_{0.33t}C_6 \rightarrow Hf_3C_2 + Al_{3.67}Si_{0.33t}$	0.351
$Hf_3Al_{3.75}Si_{0.25t}C_6 \rightarrow Hf_3C_2 + Al_{3.75}Si_{0.25t}$	0.418

To understand the underlying mechanisms why the silicon alloying reduces the adhesive energy, the bond strengths in the vicinity of the etching interface are investigated. Since our compound $Hf_3Al_4C_6$ is mostly ionic material (shown in Figure S7), and the strength of an ionic bond is proportional to the atomic charge and reverse to the bond length for a giving bond,[46] thus the atomic charge for each atom and relevant bond lengths are studied. After introducing silicon, we find that the atomic charges of the Hf and C atoms are decreased, and the bond lengths of Hf-C are increased. As a consequence, the bond strength of the Hf-C is significantly decreased. Going a step further, the adhesive energy is reduced. The relevant values and detailed discussions are given in the supporting information. The weakening of the bond strength of Hf-C can be ascribed to the larger atomic charge of silicon (2.36) than that of aluminum (2.19) (shown in Table S1), thus the shared carbon layer are bonded much stronger with the aluminum layer, which weakens the adhesive energy of the neighbouring etching interface.

The intrinsic physical properties of the as-synthesized $Hf_3C_2T_2$ (T = O, F, OH) MXenes are studied further in theoretical way. Firstly, the stable structures of these MXenes are investigated. Follow the work of Khazaei *et al.*,[23] six different structural models are studied as shown in

Figure S8, and their total energies are given in Table S2. It is found that Model II with the functional groups T on the top-sites of the hafnium atoms in the middle hafnium layer is the most stable configuration, regardless of functional groups. Based on the predicted stable configurations, the electronic, electrical and mechanical properties are studied. The structural parameters and elastic constants in the basal plane are given in Table 2, while the electronic energy bands and the electrical conductivities are given in Figure 5.

Table 2. The lattice parameters, layer thickness, and elastic constants of the $Hf_3C_2T_2$ (T=O, F, OH) MXenes.

System	Lattice parameter(Å)	Layer thickness(Å)	c_{11} (GPa)	c_{12} (GPa)
$Ti_3C_2O_2$	3.04	9.83	370	107
$Hf_3C_2O_2$	3.27	9.90	417	113
$Hf_3C_2F_2$	3.29	10.10	318	90.9
$Hf_3C_2(OH)_2$	3.30	11.80	287	67.2

From the table, $Hf_3C_2O_2$ presents smaller structural parameters and much larger elastic constants compared to $Hf_3C_2F_2$ and $Hf_3C_2(OH)_2$, similar to many other MXenes,[26] the c_{11} of $Hf_3C_2O_2$ is determined to be as high as 417 GPa. The high mechanical strength in the basal plane and the relatively thin layer thickness may partly explain the observed flexibility of this MXenes.[47] From Figure 5, all the three MXenes are metallic, and the predicted electrical conductivities σ_{xx}/τ are of the order of $10^{20}\ \Omega^{-1}m^{-1}s^{-1}$.

We further explored the feasibility of using delaminated $Hf_3C_2T_z$ (d-$Hf_3C_2T_z$) MXene flakes-based as anodes in lithium-ion batteries (LIBs) and sodium-ion batteries (SIBs). In most cases, the gravimetric capacity has been the main focus to evaluate the performance of electrodes. However, the volumetric capacity is much more important than gravimetric capacity for applications where size matters, such as wearable or portable electronics, automotive

batteries.[48, 49] Figure 6a displays the cycling performance and coulombic efficiency of the *d*-$Hf_3C_2T_z$ MXene anodes. The first discharge volumetric capacity and coulombic efficiency (orange triangle and green diamond) of *d*-$Hf_3C_2T_z$ in LIBs at a current density of 200 mAg^{-1} are 1554 mAh cm^{-3} (145 mAh g^{-1}), 59%, respectively. Then, there is a slight drop in volumetric capacity. After initial 50 cycles, it can be observed that the reversible capacity of the as-prepared electrodes is slowly increasing, and the volumetric capacity increased back to 1567 mAh cm^{-3} (146 mAh g^{-1}) at the 200th cycle, which is higher than that of the $Ti_3C_2T_z$ (640 mAh cm^{-3}) measured under the same conditions (Figure S10a). According to the reference predicted previously,[50] a maximum of 4 Li/per formula MXene can be achieved, thus a theoretical capacity of 1854 mAh cm^{-3} (173 mAh g^{-1}) can be expected. The capacities increased with increasing cycles, this effect has been observed in previously reported work on MXene, which can be attributed to the exposure of increased electrochemically active sites with prolonged cycling.[49, 51] The coulombic efficiencies approach more than 99% after the 20th cycle. There is a large irreversible capacity in the initial cycle, which can be ascribed to the solid electrolyte interface (SEI) formation on the electrode surface as well as the irreversible reduction of electrochemically active surface groups,[50] and similar behaviors have been observed for the previously reported $Ti_3C_2T_z$ and Ti_2CT_z MXenes.[52, 53] In fact, the formation of the SEI further limits electrolyte decomposition to improve the cycle life performance of the cell. Figure 6c shows the typical discharge/charge profiles of the anode electrode for the 1st, 2nd, 50th,100th, and 200th cycles at a current density of 200 mAg^{-1} in a voltage range of 0.01~3.0 V, respectively. A broad irreversible plateau, which was observed near 0.6 V (vs. Li/Li^+) during the first lithiation cycle, is most probably due to a formation of a SEI layer, as the peak does not appear in the following cycles. The irreversible reaction of Li with hydroxyl or fluorine on the surfaces of

d-$Hf_3C_2T_z$ flakes can also contribute to the first cycle irreversibility.[51] The *d*-$Hf_3C_2T_z$ MXene-based anode exhibited respectable volumetric capacities, which is comparable to what was reported for Sn^{4+} ion decorated Ti_3C_2 nanocomposites (PVP-Sn(IV)@Ti_3C_2, 1375 mAh cm^{-3} after 50cycles at 100 mA g^{-1}),[54] and is higher than that of commercial graphite electrode (550 mAh cm^{-3}).[54] The cycling performance and coulombic efficiency of *d*-$Hf_3C_2T_z$ MXene-based anodes in SIBs at a current density of 200 mAg^{-1} were also drawn in Figure 6a (blue triangle and blue square), the *d*-$Hf_3C_2T_z$ anode has a maximum capacity of 1468 mAh cm^{-3} (137 mAh g^{-1}) in the first cycle. Then the specific capacity decreases gradually, and a volumetric capacity of about 504 mAh cm^{-3} (47 mAh g^{-1}) can be maintained after 200 cycles, and which is slightly higher than that of $Ti_3C_2T_z$ (427 mAh cm^{-3}) when tested under the same conditions (Figure S10b). The improved performance of $Hf_3C_2T_z$ could be caused by the larger atomic charge of hafnium than that of titanium,[24] and the relatively higher Li/Na adsorption energy of the Hf-containing MXene.[50] Moreover, the relatively high ratio of oxygen terminations as shown in the XPS results could also be beneficial for the Li/Na capacities of $Hf_3C_2T_z$.[55] The corresponding galvanostatic charge/discharge profiles of the electrodes for SIBs measured in the potential range of 0.01~3.0 V are presented in Figure 6d. The first discharge of *d*-$Hf_3C_2T_z$ exhibited a clear plateau at around 0.75 V, which might be ascribed to the formation of SEI film. The first discharge/charge capacities are 1468/563 mAh cm^{-3}, which corresponds to the initial coulombic efficiency of 39.8%. Initial high discharge capacity and large irreversible capacity of the electrodes indicate formation of SEI and irreversible Na^+ loss.[49] When charged / discharged in SIBs under a current density of 50 mAg^{-1}, a reversible sodium intercalation capacity of 815 mAh cm^{-3} (76 mAh g^{-1}) can be reached (Figure 6a, red square and pink circle), From Fig. 6e, we can find that the charge/discharge curves of SIBs at a current density of 50 mA g^{-1} also show a steep slope and an

indistinct plateau. A large irreversible capacity of about 1318 mAh cm^{-3} (123 mAh g^{-1}) is observed during the first discharge-charge process. This irreversibility could be minimized by controlling the surface chemistry of the MXenes.[56] To effectively activating the electrode material,[16] more appropriate electrolytes should be considered to further improve the coulombic efficiency.[57]

To further assess the performance of this *d*-$Hf_3C_2T_z$ MXene-based electrode, rate cycling performance in SIBs was tested. As shown in Figure 6b, a highly symmetric pattern was obtained for the electrode discharged at various current densities (except for the first cycle due to the irreversible capacity loss). Similar to $Ti_3C_2T_z$ and Ti_2CT_z,[58, 59] the *d*-$Hf_3C_2T_z$ material showed a very good rate performance. Even at 1 Ag^{-1}, the electrode had a stable charge/discharge cycle with no obvious of capacity loss (the volumetric capacity was 312 mAh cm^{-3} after ten cycles at 1Ag^{-1}), which suggests the improved structural/chemical stability of this interleaved architecture. When the current density comes back to 50 mAg^{-1}, the volumetric capacity (733 mAh cm^{-3}) is higher than that of the initial (683 mAh cm^{-3}), indicating that the structure of the material has not been damage. The very preliminary results show that *d*-$Hf_3C_2T_z$ MXene material is a candidate anode for Na-ion storage. It is reasonable to assume that a better electrochemical performance can be obtained through further attempts, such as using hybridization strategy to improve accessibility for electrolyte, and by optimizing and engineering the surface chemistry, structure and composition of the *d*-$Hf_3C_2T_z$ MXene-based electrodes.[56, 60]

Conclusions

In summary, we successfully synthesized a 2D hafnium-containing $Hf_3C_2T_z$ MXene by selective etching of Si-alloyed Al-C sub-layer from the parent $Hf_3[Al(Si)]_4C_6$ compound. Adhesive energy and atomic charge-based calculations well revealed the underlying mechanisms

of the Si-facilitated etching process. The valance electrons in Si atom strengthened the Al(Si)-C bonding and weakened the adhesive energy of the Hf-C in the vicinity of the etching interface in $Hf_3[Al(Si)]_4C_6$. In addition, the structural, mechanical, and electronic properties of the as-obtained $Hf_3C_2T_z$ MXenes have been predicted based on first-principles density functional calculations. All of simulated $Hf_3C_2T_2$ (T = O, F, OH) MXenes are metallic with good electrical conductivity, and $Hf_3C_2O_2$ presents the strongest mechanical strength with the c_{11} value of 417 GPa. Electrochemical measurements indicated that the charge storage in d-$Hf_3C_2T_z$ was due to the intercalation of Li^+ and Na^+ ions rather than a conversion reaction. It exhibited reversible volumetric capacities of 1567 mAh cm^{-3} and 504 mAh cm^{-3} for lithium and sodium ions batteries at a current density of 200 mAg^{-1}, respectively. These results suggest that d-$Hf_3C_2T_z$ with 2D structure is a candidate anode material for metal-ion intercalation, especially for applications where size matters. Moreover, our obtained $Hf_3C_2T_z$ MXene that has abundant electrons may be important for catalysis and electromagnetic interference shielding applications beyond energy storage.

Methods/experimental

Materials: The $Hf_3[Al(Si)]_4C_6$ powders were prepared by pulsed electric current sintering (PECS) of Hf/Al/Si/graphite powder mixtures with a molar ratio of Hf:Al:Si:C, 3:4.05:0.15:5.8, respectively. In detail, the weighted powders were blended in a polyethylene jar for 16 h in a planetary ball mill at a rate of 250 rpm with absolute ethanol and agate balls as grinding media. The powder mixture was then dried in vacuum oven at 40°C for 24 h. Subsequently, the resulting powders were poured into a graphite die (20 mm in diameter) and cold pressed to load corresponding to a pressure of 5 MPa, and the sample was heated in a PECS apparatus (HP D25/1, FCT Systeme GmbH, Germany) to1900°C for 20 min with holding pressure of 5Mpa in

an Ar atmosphere, and then vacuum annealing was employed at 1600℃ for 10min during the cooling process. After cooling to room temperature, bulk samples were pulverized and sieved through a 300-mesh screen. The Hf-Al-C powders were made by mixing elemental Hf/Al/graphite, in the molar ratio of 3:3.2:4.8, respectively, in a ball mill for 12 h. The mixed powders were then heated 50 °C /min to 1900°C and held at that temperature in a PECS apparatus (HP D25/1, FCT Systeme GmbH, Germany) for 20 min with holding pressure of 5Mpa in an Ar atmosphere. After cooling to room temperature, powders were produced by milling as above.Roughly 1g of the as-prepared 300-mesh $Hf_3[Al(Si)]_4C_6$ powders was immersed in 35 wt % HF (10 ml) solution at room temperature for about 60 h, and the overall yield was around 73% (defined as the weight of powder after HF treatment/ weight of the pristine powder × 100%). In the case of Hf-Al-C system, powders were immersed at room temperature in HF solutions of varying potency for various times, Table S3 summarizes the times and concentrations used. Then the resulting suspension was cleaned by deionized water and alcohol for several times and filtered with microfiltration membrane (polyvinylidene fluoride，PVDF, 0.45μm, Shanghai Xinya) to separate the powders. The final product was finally dried in vacuum oven at room temperature for 48 h. For SEM, AFM and TEM characterization of the etching product from $Hf_3[Al(Si)]_4C_6$ precursor, the as-etched powders were mixed with distilled water (0.25g in 25mL distilled water), sonicating under Ar to prevent oxidation for about 20min (working frequency:53kHz; full power: 250watts; Shanghai Kudos Ultrasonic Instrument co., LTD; and 60% of the power was used during the sonication process), and centrifuging at 2500 rpm for 5 min to separate large unreacted particles, and finally decanted (~2mg/mL). The suspension was then re-dispersed in 75mL distilled water, sonication under Ar to prevent oxidation for another 30-40min, centrifuging at 5000rpm

for 30min, and decanted to obtain the final stable colloidal solution of delaminated $Hf_3C_2T_z$ flakes (~0.3mg/mL). Then droplets from the supernatant were left to dry on a silicon wafer (p(100) oriented) for SEM and AFM study, and on a lacey-carbon coated copper grid (200 mesh) for TEM study, respectively.

Characterization: The phase composition of the as-prepared samples was analyzed by X-ray diffractometry, XRD, (D8 Advance, Bruker AXS, Germany) with Cu K_α radiation. X-ray diffractograms were collected at a step size of 0.02° 2θ with a collection time of 1s per step. The microstructure and chemical composition were observed by Field Emission Scanning Electron Microscope, FESEM (QUANTA 250 FEG, FEI, USA) coupled with an energy dispersive spectrometer (EDS). The chemical state of the materials before and after exfoliation was analyzed by X-ray photoelectron spectroscopy, XPS (AXISUltra DLD, Kratos, Japan). Transmission electron microscopy (TEM) and high-resolution TEM images were carried out on a Tecnai F20 (FEI, USA) electron microscope at an acceleration voltage of 200 kV. Atomic force microscopy (AFM) analysis was performed by means of Dimension 3100V system (Veeco, USA) under tapping mode.

Preparation and Testing of LIB and NIB Electrodes: Working electrodes were fabricated by standard slurry casting procedure. The as-etched powders were mixed with distilled water (0.5g in 50mL distilled water), sonicating for about 20min, and centrifuging at 2500 rpm for 5 min to separate large unreacted particles, and finally decanted. The suspension was then re-dispersed in 150mL distilled water, sonication for another 30-40min, centrifuging at 5000rpm for 30min, and decanted. The colloidal suspension was finally filtered with microfiltration membrane (polyvinylidene fluoride , PVDF, 0.20μm,

Shanghai Xinya), and dried in vacuum oven at room temperature for 48 h, and the obtained powders of delaminated $Hf_3C_2T_z$ flakes (*d*-$Hf_3C_2T_z$) was used to prepare anodes. *d*-$Hf_3C_2T_z$ (70 wt %), conductive carbon black (Super P carbon 20 wt %) and polyvinylidene fluoride (PVDF 10 wt %) were intimately mixed in N−methyl-2-pyrrolidone (NMP) to form a uniform slurry. Then the casted film (on Cu foil) was heated at 110 ^{o}C for 12 h in a vacuum oven to evaporate the solvent. After cooling down to room temperature, and cut into circular discs of 15 mm in diameter. The loaded mass of the anode is in the range of 0.5-0.7 mg (average thickness ~4 μm). Metallic lithium foil was used as counter as well as reference electrode. Celgard 2400 polypropylene film was used as a separator. Electrolyte was prepared by dissolving 1 M lithium hexafluorophosphate ($LiPF_6$) in a mixture of ethylene carbonate /dimethyl carbonate (EC:DMC, 1:1 by volume) and supplemented by 10 vol% of fluoroethylene carbonate (FEC). There is a little difference between lithium and sodium batteries. In sodium batteries, metallic sodium foil was used as counter as well as reference electrode. Whatman Glass Fiber was used as a separator. Electrolyte was prepared by dissolving 1 M sodium perchlorate ($NaClO_4$) in Tetraethylene glycol dimethy ether. Finally, all the cells were assembled in an argon-filled glove box, where water and oxygen concentrations were limited to below 0.1 ppm. Charge/discharge measurements of the coin cells were carries out using a commercial battery test system (LAND model, CT2001A) at a constant current in the potential range of 0.01~3.00 V(vs.Li/Li^+; Na/Na^+). The volume capacity was converted from the measured gravimetric capacity through the estimated density of active material delaminated $Hf_3C_2T_z$ with oxygen termination ($Hf_3C_2O_2$, 10.72g/cm^3).

Computational details: All the first-principles calculations are implemented in the plane-wave VASP code. The energy cutoffs are set to 500 eV in describing the electronic

wavefunctions based on the projected augmented wave (PAW) approach. The generalized gradient approximation (GGA) authored by Purdue-Burke-Ernzerhof (PBE) is used to describe the exchange and correlation functional. During optimization, all the structures are relaxed until the forces on each atom are smaller than 1.0×10^{-4} eV/Å, and the criterion for energy convergence is set as 1.0×10^{-5} eV. To simulate the 2D MXenes and monomers discussed in the main text, a vacuum space at least 15 Å is adopted along the direction perpendicular to the surface. A Γ-centered $12 \times 12 \times 1$ k-point mesh is employed to describe the entire Brillouin zone (BZ). For optimizations of the multilayer MXenes, a $12 \times 12 \times 4$ k-point mesh is adopted. In order to investigate the bonding behaviors in the vicinity of the layers where etching occurred, the corresponding atomic charge and bond lengths are studied. The Bader charge analysis based on a $180 \times 180 \times 1$ grid is performed. The electrical conductivity is obtained from Boltzmann theory implemented in the BoltzTraP code, the corresponding energy files are calculated based on a 80 $\times 80 \times 1$ k-points mesh. All the structures are visualized in the VESTA code.

Supporting Information

High-resolution XPS spectra of samples before and after etching treatment in the Hf 4f region, in the O 1s region, in the C 1s region, in the Al 2p and Si 2p region. The EDS results as-synthesized $Hf_3[Al(Si)]_4C_6$ powders, HF-etched powders and delaminated $Hf_3C_2T_z$ flakes. Side-views of multilayer $Ti_3C_2F_2$ and $Hf_3C_2F_2$ MXene before and after optimization. The electronic density distribution of the $Hf_3Al_4C_6$ monomer, the atomic charges and corresponding bond lengths near the breaking bonds in $Hf_3Al_4C_6$ and $Hf_3Al_{3.5}Si_{0.5t}C_6$. The side-views of six different structural models of the as-synthesized $Hf_3C_2T_2$ (T = O, F, OH) MXenes. The total energies of different models for $Hf_3C_2T_2$ (T = O, F, OH) MXenes. Exfoliation process parameters of Hf-Al-C composite powders.

Corresponding Authors

*E-mail (Qing Huang): huangqing@nimte.ac.cn.
*E-mail (Shiyu Du): dushiyu@nimte.ac.cn.
*E-mail (Cai Shen): shencai@nimte.ac.cn.

Author Contributions

† These authors contributed equally to this work.

Acknowledgements

The present work was supported by the National Natural Science Foundation of China (Grant Nos. 21671195, 11604346, 51502310, 21577144 and 91426304), ITaP at Purdue University for computing resources, the key technology of nuclear energy, 2014, CAS Interdisciplinary Innovation Team. P. Eklund also acknowledges the Swedish Foundation for Strategic Research (SSF) through the Future Research Leaders 5 program and the Synergy Grant FUNCASE. The authors thank Guoxin Chen for the TEM characterization and thank Kemin Jiang for the XPS analysis of Hafnium-containing MXenes.

References

(1) Novoselov, K. S.; Geim, A. K.; Morozov, S. V.; Jiang, D.; Zhang, Y.; Dubonos, S. V.; Grigorieva, I. V.; Firsov, A. A., Electric Field Effect in Atomically Thin Carbon Films. *Science* **2004,** *306*, 666-669.

(2) Zhu, Y.; Murali, S.; Cai, W.; Li, X.; Suk, J. W.; Potts, J. R.; Ruoff, R. S., Graphene and Graphene Oxide: Synthesis, Properties, and Applications. *Adv. Mater.* **2010,** *22*, 3906-3924.

(3) Ma, R.; Sasaki, T., Nanosheets of Oxides and Hydroxides: Ultimate 2D Charge-Bearing Functional Crystallites. *Adv. Mater.* **2010,** *22*, 5082-5104.

(4) Wang, Q. H.; Kalantar-Zadeh, K.; Kis, A.; Coleman, J. N.; Strano, M. S., Electronics and Optoelectronics of Two-Dimensional Transition Metal Dichalcogenides. *Nat Nano* **2012,** *7*, 699-712.

(5) Ci, L.; Song, L.; Jin, C.; Jariwala, D.; Wu, D.; Li, Y.; Srivastava, A.; Wang, Z. F.; Storr, K.; Balicas, L.; Liu, F.; Ajayan, P. M., Atomic Layers of Hybridized Boron Nitride and Graphene Domains. *Nat Mater* **2010,** *9*, 430-435.

(6) Butler, S. Z.; Hollen, S. M.; Cao, L.; Cui, Y.; Gupta, J. A.; Gutiérrez, H. R.; Heinz, T. F.; Hong, S. S.; Huang, J.; Ismach, A. F.; Johnston-Halperin, E.; Kuno, M.; Plashnitsa, V. V.; Robinson, R. D.; Ruoff, R. S.; Salahuddin, S.; Shan, J.; Shi, L.; Spencer, M. G.; Terrones, M., *et al*., Progress, Challenges, and Opportunities in Two-Dimensional Materials Beyond Graphene. *ACS nano* **2013,** *7*, 2898-2926.

(7) Naguib, M.; Kurtoglu, M.; Presser, V.; Lu, J.; Niu, J.; Heon, M.; Hultman, L.; Gogotsi, Y.; Barsoum, M. W., Two-Dimensional Nanocrystals Produced by Exfoliation of Ti_3AlC_2. *Adv. Mater.* **2011,** *23*, 4248-4253.

(8) Naguib, M.; Mashtalir, O.; Carle, J.; Presser, V.; Lu, J.; Hultman, L.; Gogotsi, Y.; Barsoum, M. W., Two-Dimensional Transition Metal Carbides. *ACS nano* **2012,** *6*, 1322-1331.

(9) Naguib, M.; Mochalin, V. N.; Barsoum, M. W.; Gogotsi, Y., Two-Dimensional Materials: 25th Anniversary Article: MXenes: A New Family of Two-Dimensional Materials (Adv. Mater. 7/2014). *Adv. Mater.* **2014,** *26*, 982-982.

(10) Naguib, M.; Gogotsi, Y., Synthesis of Two-Dimensional Materials by Selective Extraction. *Acc. Chem. Res.* **2015,** *48*, 128-135.

(11) Barsoum, M. W., The $M_{n+1}AX_n$ Phases: A New Class of Solids; Thermodynamically Stable Nanolaminates. *Prog. Solid State Chem.* **2000,** *28*, 201-281.

(12) Urbankowski, P.; Anasori, B.; Makaryan, T.; Er, D.; Kota, S.; Walsh, P. L.; Zhao, M.; Shenoy, V. B.; Barsoum, M. W.; Gogotsi, Y., Synthesis of Two-Dimensional Titanium Nitride Ti_4N_3 (MXene). *Nanoscale* **2016,** *8*, 11385-11391.

(13) Zhou, J.; Zha, X.; Chen, F. Y.; Ye, Q.; Eklund, P.; Du, S.; Huang, Q., A Two-Dimensional Zirconium Carbide by Selective Etching of Al_3C_3 from Nanolaminated $Zr_3Al_3C_5$. *Angew. Chem. Int. Ed.* **2016,** *55*, 5008-5013.

(14) Anasori, B.; Xie, Y.; Beidaghi, M.; Lu, J.; Hosler, B. C.; Hultman, L.; Kent, P. R. C.; Gogotsi, Y.; Barsoum, M. W., Two-Dimensional, Ordered, Double Transition Metals Carbides (MXenes). *ACS nano* **2015,** *9*, 9507-9516.

(15) Ghidiu, M.; Naguib, M.; Shi, C.; Mashtalir, O.; Pan, L. M.; Zhang, B.; Yang, J.; Gogotsi, Y.; Billinge, S. J. L.; Barsoum, M. W., Synthesis and Characterization of Two-Dimensional Nb_4C_3 (MXene). *Chem. Commun.* **2014,** *50*, 9517-9520.

(16) Naguib, M.; Halim, J.; Lu, J.; Cook, K. M.; Hultman, L.; Gogotsi, Y.; Barsoum, M. W., New Two-Dimensional Niobium and Vanadium Carbides as Promising Materials for Li-Ion Batteries. *J. Am. Chem. Soc.* **2013,** *135*, 15966-15969.

(17) Halim, J.; Kota, S.; Lukatskaya, M. R.; Naguib, M.; Zhao, M. Q.; Moon, E. J.; Pitock, J.; Nanda, J.; May, S. J.; Gogotsi, Y., Synthesis and Characterization of 2D Molybdenum Carbide (MXene). *Adv. Funct. Mater.* **2016,** *26*, 3118-3127.

(18) Meshkian, R.; Näslund, L.-Å.; Halim, J.; Lu, J.; Barsoum, M. W.; Rosen, J., Synthesis of Two-Dimensional Molybdenum Carbide, Mo_2C, from the Gallium Based Atomic Laminate Mo_2Ga_2C. *Scripta Mater.* **2015,** *108*, 147-150.

(19) Xu, C.; Wang, L.; Liu, Z.; Chen, L.; Guo, J.; Kang, N.; Ma, X.-L.; Cheng, H.-M.; Ren, W., Large-Area High-Quality 2D Ultrathin Mo_2C Superconducting Crystals. *Nat Mater* **2015,** *14*, 1135-1141.

(20) Yang, J.; Naguib, M.; Ghidiu, M.; Pan, L.-M.; Gu, J.; Nanda, J.; Halim, J.; Gogotsi, Y.; Barsoum, M. W., Two-Dimensional Nb-Based M_4C_3 Solid Solutions (MXenes). *J. Am. Ceram. Soc.* **2016,** *99*, 660-666.

(21) Meshkian, R.; Tao, Q.; Dahlqvist, M.; Lu, J.; Hultman, L.; Rosen, J., Theoretical Stability and Materials Synthesis of a Chemically Ordered MAX Phase, Mo_2ScAlC_2, and Its Two-Dimensional Derivate Mo_2ScC_2

MXene. *Acta Mater.* **2017,** *125*, 476-480.

(22) Coleman, J. N.; Lotya, M.; O'Neill, A.; Bergin, S. D.; King, P. J.; Khan, U.; Young, K.; Gaucher, A.; De, S.; Smith, R. J.; Shvets, I. V.; Arora, S. K.; Stanton, G.; Kim, H.-Y.; Lee, K.; Kim, G. T.; Duesberg, G. S.; Hallam, T.; Boland, J. J.; Wang, J. J., *et al.*, Two-Dimensional Nanosheets Produced by Liquid Exfoliation of Layered Materials. *Science* **2011,** *331*, 568-571.

(23) Khazaei, M.; Arai, M.; Sasaki, T.; Chung, C.-Y.; Venkataramanan, N. S.; Estili, M.; Sakka, Y.; Kawazoe, Y., Novel Electronic and Magnetic Properties of Two-Dimensional Transition Metal Carbides and Nitrides. *Adv. Funct. Mater.* **2013,** *23*, 2185-2192.

(24) Zha, X.-H.; Huang, Q.; He, J.; He, H.; Zhai, J.; Francisco, J. S.; Du, S., The Thermal and Electrical Properties of the Promising Semiconductor MXene Hf_2CO_2. *Scientific Reports* **2016,** *6*, 27971.

(25) Zha, X.-H.; Zhou, J.; Zhou, Y.; Huang, Q.; He, J.; Francisco, J. S.; Luo, K.; Du, S., Promising Electron Mobility and High Thermal Conductivity in Sc_2CT_2 (T = F, OH) MXenes. *Nanoscale* **2016,** *8*, 6110-6117.

(26) Zha, X. H.; Luo, K.; Li, Q.; Huang, Q.; He, J.; Wen, X.; Du, S., Role of the Surface Effect on the Structural, Electronic and Mechanical Properties of the Carbide MXenes. *EPL (Europhysics Letters)* **2015,** *111*, 26007.

(27) Tang, Q.; Zhou, Z.; Shen, P., Are MXenes Promising Anode Materials for Li Ion Batteries? Computational Studies on Electronic Properties and Li Storage Capability of Ti_3C_2 and $Ti_3C_2X_2$ (X = F, OH) Monolayer. *J. Am. Chem. Soc.* **2012,** *134*, 16909-16916.

(28) Lukatskaya, M. R.; Mashtalir, O.; Ren, C. E.; Dall'Agnese, Y.; Rozier, P.; Taberna, P. L.; Naguib, M.; Simon, P.; Barsoum, M. W.; Gogotsi, Y., Cation Intercalation and High Volumetric Capacitance of Two-Dimensional Titanium Carbide. *Science* **2013,** *341*, 1502-1505.

(29) Ghidiu, M.; Lukatskaya, M. R.; Zhao, M.-Q.; Gogotsi, Y.; Barsoum, M. W., Conductive Two-Dimensional Titanium Carbide 'Clay' with High Volumetric Capacitance. *Nature* **2014,** *516*, 78-81.

(30) Xu, B.; Zhu, M.; Zhang, W.; Zhen, X.; Pei, Z.; Xue, Q.; Zhi, C.; Shi, P., Field-Effect Transistors: Ultrathin MXene-Micropattern-Based Field-Effect Transistor for Probing Neural Activity. *Adv. Mater.* **2016,** *28*, 3411-3411.

(31) Seh, Z. W.; Fredrickson, K. D.; Anasori, B.; Kibsgaard, J.; Strickler, A. L.; Lukatskaya, M. R.; Gogotsi,

Y.; Jaramillo, T. F.; Vojvodic, A., Two-Dimensional Molybdenum Carbide (MXene) as an Efficient Electrocatalyst for Hydrogen Evolution. *ACS Energy Lett.* **2016,** *1*, 589-594.

(32) Boota, M.; Anasori, B.; Voigt, C.; Zhao, M.-Q.; Barsoum, M. W.; Gogotsi, Y., Pseudocapacitive Electrodes Produced by Oxidant-Free Polymerization of Pyrrole between the Layers of 2D Titanium Carbide (MXene). *Adv. Mater.* **2016,** *28*, 1517-1522.

(33) Chen, J.; Chen, K.; Tong, D.; Huang, Y.; Zhang, J.; Xue, J.; Huang, Q.; Chen, T., CO_2 and Temperature Dual Responsive "Smart" MXene Phases. *Chem. Commun.* **2015,** *51*, 314-317.

(34) Lapauw, T.; Lambrinou, K.; Cabioc'h, T.; Halim, J.; Lu, J.; Pesach, A.; Rivin, O.; Ozeri, O.; Caspi, E. N.; Hultman, L.; Eklund, P.; Rosén, J.; Barsoum, M. W.; Vleugels, J., Synthesis of the New MAX Phase Zr_2AlC. *J. Eur. Ceram. Soc.* **2016,** *36*, 1847-1853.

(35) Lapauw, T.; Halim, J.; Lu, J.; Cabioc'h, T.; Hultman, L.; Barsoum, M. W.; Lambrinou, K.; Vleugels, J., Synthesis of the Novel Zr_3AlC_2 MAX phase. *J. Eur. Ceram. Soc.* **2016,** *36*, 943-947.

(36) Lapauw, T.; Tunca, B.; Cabioc'h, T.; Lu, J.; Persson, P. O. Å.; Lambrinou, K.; Vleugels, J., Synthesis of MAX Phases in the Hf–Al–C System. *Inorg. Chem.* **2016**.

(37) Zhou, Y.-C.; He, L.-F.; Lin, Z.-J.; Wang, J.-Y., Synthesis and Structure–Property Relationships of a New Family of Layered Carbides in Zr-Al(Si)-C and Hf-Al(Si)-C Systems. *J. Eur. Ceram. Soc.* **2013,** *33*, 2831-2865.

(38) Zhang, X.; Xu, J.; Wang, H.; Zhang, J.; Yan, H.; Pan, B.; Zhou, J.; Xie, Y., Ultrathin Nanosheets of Max Phases with Enhanced Thermal and Mechanical Properties in Polymeric Compositions: TiSiAlC. *Angew. Chem. Int. Ed.* **2013,** *52*, 4361-4365.

(39) He, L. F.; Nian, H. Q.; Lu, X. P.; Bao, Y. W.; Zhou, Y. C., Mechanical and Thermal Properties of a $Hf_2[Al(Si)]_4C_5$ Ceramic Prepared by *in situ* Reaction/Hot-Pressing. *Scripta Mater.* **2010,** *62*, 427-430.

(40) Zhou, J.; Qiu, F.; Shen, L.; Li, F.; Xue, J.; Barsoum, M. W.; Huang, Q., Pulse Electric Current–Aided Reactive Sintering of High-Purity $Zr_3Al_3C_5$. *J. Am. Ceram. Soc.* **2014,** *97*, 1296-1302.

(41) Mashtalir, O.; Naguib, M.; Mochalin, V. N.; Dall'Agnese, Y.; Heon, M.; Barsoum, M. W.; Gogotsi, Y., Intercalation and Delamination of Layered Carbides and Carbonitrides. *Nat Commun* **2013,** *4*, 1716.

(42) Halim, J.; Cook, K. M.; Naguib, M.; Eklund, P.; Gogotsi, Y.; Rosen, J.; Barsoum, M. W., X-Ray

Photoelectron Spectroscopy of Select Multi-Layered Transition Metal Carbides (MXenes). *Appl. Surf. Sci.* **2016,** *362*, 406-417.

(43) Naguib, M.; Unocic, R. R.; Armstrong, B. L.; Nanda, J., Large-Scale Delamination of Multi-Layers Transition Metal Carbides and Carbonitrides "MXenes". *Dalton Transactions* **2015,** *44*, 9353-9358.

(44) Kim, S. J.; Choi, K.; Lee, B.; Kim, Y.; Hong, B. H., Materials for Flexible, Stretchable Electronics: Graphene and 2D Materials. *Annu. Rev. Mater. Res.* **2015,** *45*, 63-84.

(45) Xian-Hu, Z.; Jie, Z.; Kan, L.; Jiajian, L.; Qing, H.; Xiaobing, Z.; Joseph, S. F.; Jian, H.; Shiyu, D., Controllable Magnitude and Anisotropy of the Electrical Conductivity of Hf $_3C_2O_2$ MXene. *J. Phys.: Condens. Matter.* **2017,** *29*, 165701.

(46) Zio´łkowski, J., New Relation between Ionic Radii, Bond Length, and Bond Strength. *J. Solid State Chem.* **1985,** *57*, 269-290.

(47) Ortiz, A. U.; Boutin, A.; Fuchs, A. H.; Coudert, F.-X., Anisotropic Elastic Properties of Flexible Metal-Organic Frameworks: How Soft Are Soft Porous Crystals? *Phys. Rev. Lett.* **2012,** *109*, 195502.

(48) Gogotsi, Y.; Simon, P., Materials Science. True Performance Metrics in Electrochemical Energy Storage. *Science* **2011,** *334*, 917-8.

(49) Xie, X.; Zhao, M.-Q.; Anasori, B.; Maleski, K.; Ren, C. E.; Li, J.; Byles, B. W.; Pomerantseva, E.; Wang, G.; Gogotsi, Y., Porous Heterostructured MXene/Carbon Nanotube Composite Paper with High Volumetric Capacity for Sodium-Based Energy Storage Devices. *Nano Energy* **2016,** *26*, 513-523.

(50) Sun, D.; Hu, Q.; Chen, J.; Zhang, X.; Wang, L.; Wu, Q.; Zhou, A., Structural Transformation of MXene (V_2C, Cr_2C, and Ta_2C) with O Groups During Lithiation: A First-Principles Investigation. *ACS Appl. Mater. Inter.* **2016,** *8*, 74-81.

(51) Zhao, M.-Q.; Torelli, M.; Ren, C. E.; Ghidiu, M.; Ling, Z.; Anasori, B.; Barsoum, M. W.; Gogotsi, Y., 2D Titanium Carbide and Transition Metal Oxides Hybrid Electrodes for Li-Ion Storage. *Nano Energy* **2016,** *30*, 603-613.

(52) Naguib, M.; Come, J.; Dyatkin, B.; Presser, V.; Taberna, P.-L.; Simon, P.; Barsoum, M. W.; Gogotsi, Y., MXene: A Promising Transition Metal Carbide Anode for Lithium-Ion Batteries. *Electrochem. Commun.* **2012,** *16*, 61-64.

(53) Sun, D.; Wang, M.; Li, Z.; Fan, G.; Fan, L.-Z.; Zhou, A., Two-Dimensional Ti_3C_2 as Anode Material for Li-Ion Batteries. *Electrochem. Commun.* **2014,** *47*, 80-83.

(54) Luo, J.; Tao, X.; Zhang, J.; Xia, Y.; Huang, H.; Zhang, L.; Gan, Y.; Liang, C.; Zhang, W., Sn^{4+} Ions Decorated Highly Conductive Ti_3C_2 MXene: Promising Lithium-Ion Anodes with Enhanced Volumetric Capacity and Cyclic Performance. *ACS nano* **2016,** *10*, 2491-2499.

(55) Xie, Y.; Naguib, M.; Mochalin, V. N.; Barsoum, M. W.; Gogotsi, Y.; Yu, X.; Nam, K.-W.; Yang, X.-Q.; Kolesnikov, A. I.; Kent, P. R. C., Role of Surface Structure on Li-Ion Energy Storage Capacity of Two-Dimensional Transition-Metal Carbides. *J. Am. Chem. Soc.* **2014,** *136*, 6385-6394.

(56) Mendoza-Sánchez, B.; Gogotsi, Y., Synthesis of Two-Dimensional Materials for Capacitive Energy Storage. *Adv. Mater.* **2016,** *28*, 6104-6135.

(57) Xu, Z.; Wang, J.; Yang, J.; Miao, X.; Chen, R.; Qian, J.; Miao, R., Enhanced Performance of a Lithium–Sulfur Battery Using a Carbonate-Based Electrolyte. *Angew. Chem. Int. Ed.* **2016,** *55*, 10372-10375.

(58) Wang, X.; Kajiyama, S.; Iinuma, H.; Hosono, E.; Oro, S.; Moriguchi, I.; Okubo, M.; Yamada, A., Pseudocapacitance of MXene Nanosheets for High-Power Sodium-Ion Hybrid Capacitors. *Nat. Commun.* **2015,** *6*, 6544.

(59) Wang, X.; Shen, X.; Gao, Y.; Wang, Z.; Yu, R.; Chen, L., Atomic-Scale Recognition of Surface Structure and Intercalation Mechanism of $Ti_3C_2T_x$. *J. Am. Chem. Soc.* **2015,** *137*, 2715-2721.

(60) Ng, V.; Huang, H.; Zhou, K.; Lee, P. S.; Que, W.; Xu, Z. J.; Kong, L. B., Recent Progress in Layered Transition Metal Carbides and/or Nitrides (MXenes) and Their Composites: Synthesis and Applications. *J. Mater. Chem. A.***2017,** *5*, 3039-3068.

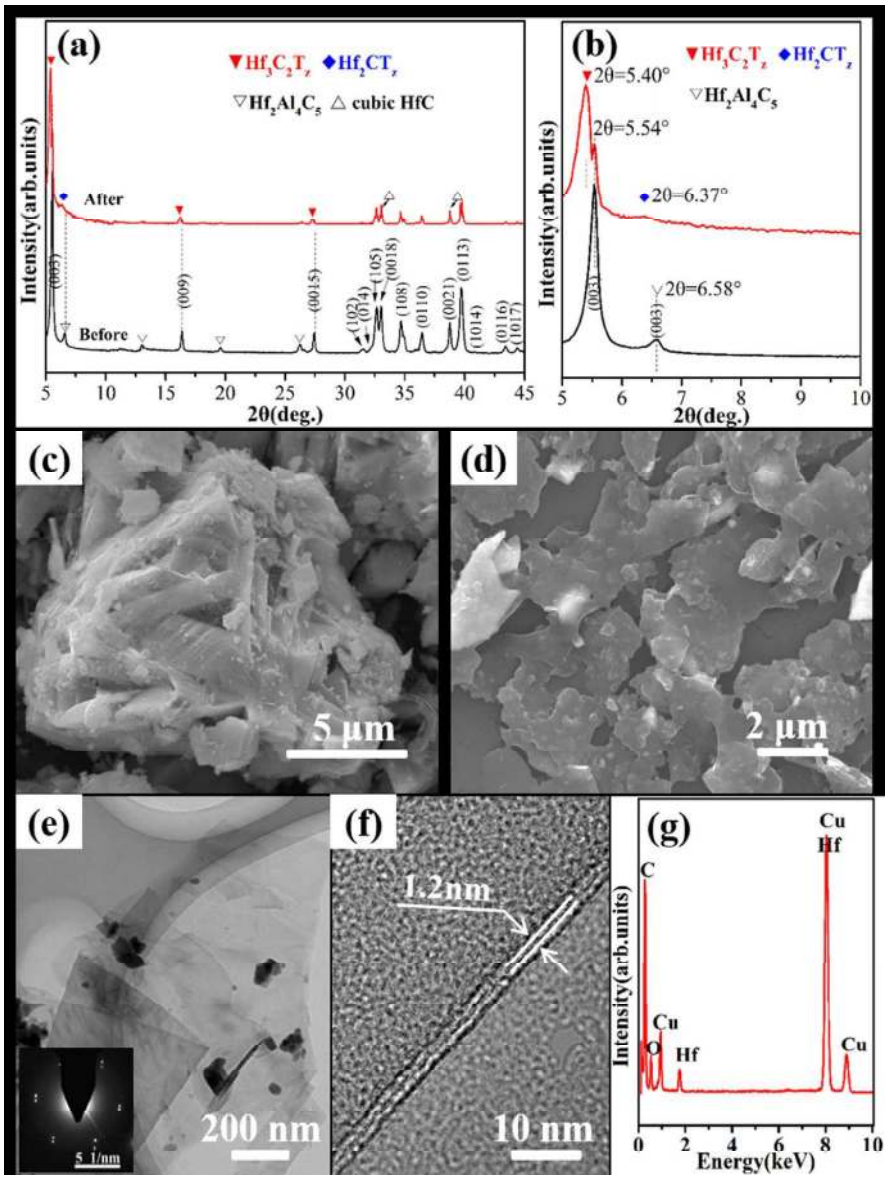

Figure 1 (a) X-ray diffraction patterns of Hf3[Al(Si)]4C6 powders before and after treatment with concentrated HF solution, and (b) is an enlarged view of the area with 2θ between 5° to 10°. (c) SEM images of as-synthesized Hf3[Al(Si)]4C6 powders, (d) SEM image of HF treated powders after sonication and centrifugation, then filtered from the aqueous suspension, showing delaminated flakes with large lateral size; (e)typical bright-field TEM images of the delaminated Hf3C2Tz flakes, depicting scrolled behavior; (f) TEM image of few layered Hf3C2Tz flakes; and (g) corresponding EDX results of the Hf3C2Tz flakes shown in (e). Left inset in (e) is a SAED pattern confirming the hexagonal basal plane symmetry.

193x256mm (300 x 300 DPI)

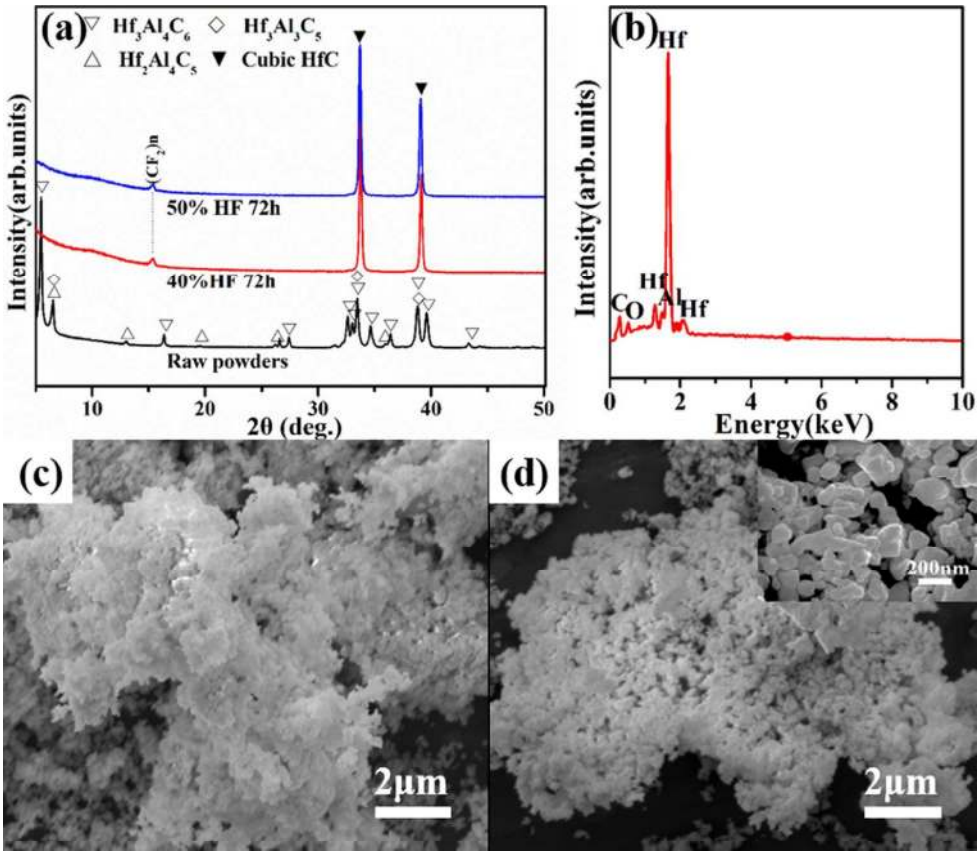

Figure 2 (a) X-ray diffraction patterns of Hf-Al-C composite powders before and after HF treatment with varied concentration, (b) the EDS results of the HF-etched powders, and the corresponding molar ratio of Hf:C approximate 1:1, (c)-(d) secondary electron SEM micrographs for Hf-Al-C composite powders after HF treatment with varied concentration, respectively, and right inset in (d) is a magnified image of the obtained cubic HfC particles.

104x90mm (300 x 300 DPI)

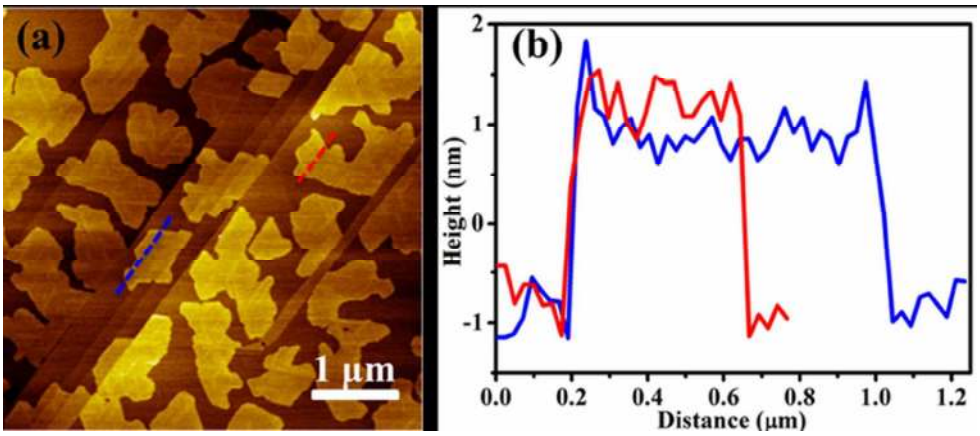

Figure 3 (a) AFM topography image of Hf3C2Tz nanosheets deposited on HOPG substrate, and (b) the corresponding height profile.

61x26mm (300 x 300 DPI)

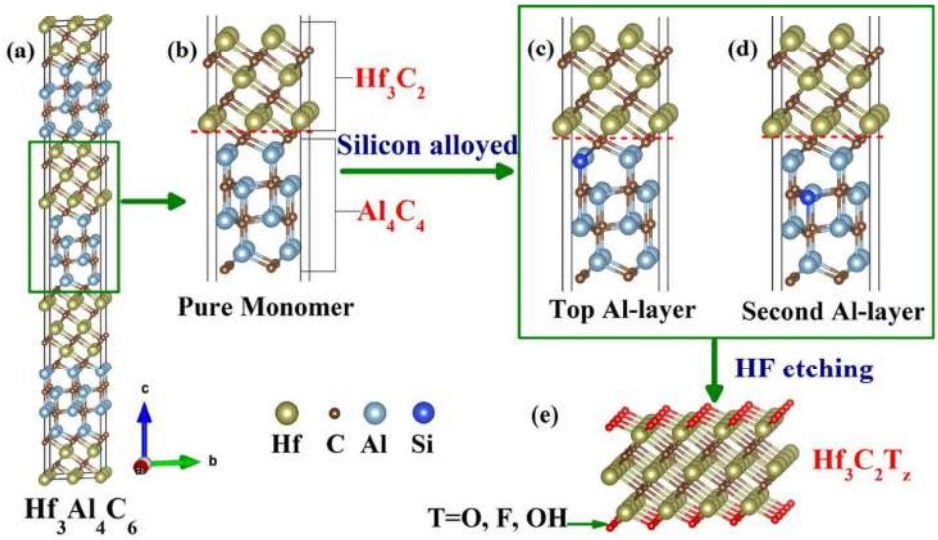

Figure 4 The schematic diagram showing the fabrication process of the Hf3C2Tz MXene (a) shows the pure Hf3Al4C6 supercell; (b) depicts the Hf3Al4C6 monomer in its supercell, where the red dashed line denotes the etching interface. (c) and (d) show the silicon alloying in the Hf3Al4C6 monomer. Two different replacement positions as (c) in the top Al-layer and (d) in the second Al-layer are presented. (e) shows the side-view of Hf3C2Tz MXene.

102x61mm (300 x 300 DPI)

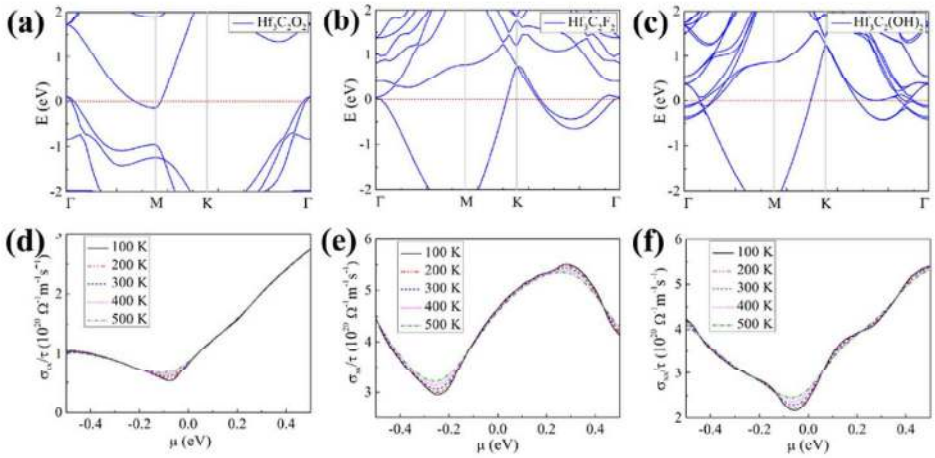

Figure 5 The electronic energy bands and electrical conductivities of the Hf3C2T2(T=O, F, OH) MXenes. (a), (b) and (c) are the electronic energy bands for Hf3C2O2, Hf3C2F2, Hf3C2(OH)2, respectively. (d), (e) and (f) represent the relationships between the values of electrical conductivity respect to scattering time and the chemical potentials, which are for Hf3C2O2, Hf3C2F2, Hf3C2(OH)2, respectively.

89x44mm (300 x 300 DPI)

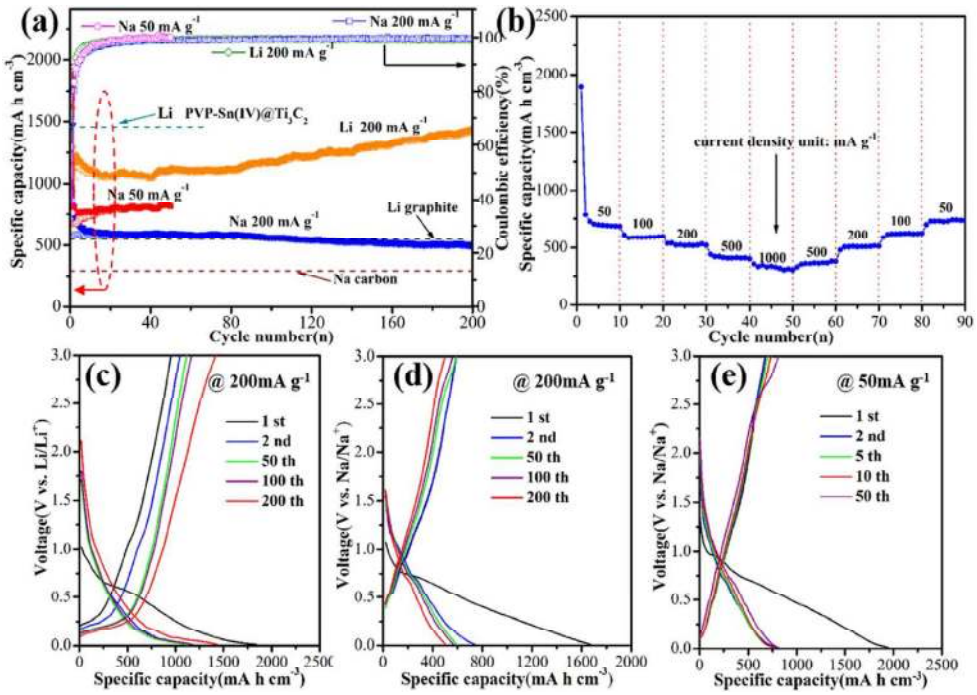

Figure 6 Electrochemical performance of d-Hf3C2Tz MXene-based electrodes. (a) Specific charge (hollow symbols), discharge (solid symbols) capacities and coulombic efficiency vs cycle number at different current densities for d-Hf3C2Tz MXene in LIBs and SIBs, respectively; (b) the rate capability of d-Hf3C2Tz MXene from 50 mA g-1 to 1 A g-1 in SIBs; (c)Voltage profile of d-Hf3C2Tz MXene between 0.01-3.0V vs Li/Li+ at a current density of 200 mA g-1; (d) and (e) Voltage profile of d-Hf3C2Tz MXene between 0.01-3.0V vs Na/Na+ at current densities of 200 mA g-1 and 50 mA g-1, respectively.

160x112mm (300 x 300 DPI)